Journal of Materials Research and Technology 33 (2024) 2731–2743

Contents lists available at ScienceDirect

Journal of Materials Research and Technology

journal homepage: www.elsevier.com/locate/jmrt

Microstructures, physical and corrosion behavior of NiCoFeCu high-entropy alloy nanocomposite coatings electro-co-deposited with nano-Si_3N_4 particles

Ying Wang [a], Bingyang Ma [a], Wei Li [b], Peter K. Liaw [c], Xiaodong Wang [d], Songpu Yang [e], Ning Zhong [e,*]

[a] School of Materials Science, Shanghai Dianji University, Shanghai, 201306, China
[b] School of Materials Science and Engineering, University of Shanghai for Science and Technology, Shanghai, 200093, China
[c] Department of Materials Science and Engineering, The University of Tennessee, Knoxville, TN, 37996-2200, USA
[d] School of Materials Science and Engineering, Shanghai JiaoTong University, Shanghai, 200240, China
[e] College of Ocean Science and Engineering, Shanghai Maritime University, Shanghai, 201306, China

ARTICLE INFO

Handling editor: L Murr

Keywords:
Electrodeposition
High-entropy alloys
Coatings
Corrosion
Microstructure

ABSTRACT

High-entropy alloys (HEAs) have gained increasing attention over the decades, owing to their distinctive properties. Electrodeposition stands out as a cost-effective and convenient method for producing diverse types of HEAs. However, there's little attention paid to fabricating ceramic-enhanced HEA composites. In this study, NiFeCoCu/Si_3N_4 HEA nanocomposites were electro-co-deposited in an aqueous solution with varying loadings of Si_3N_4 nanoparticles and current densities. The morphological, elemental, and phase-structure characteristics were investigated using scanning electron microscopy (SEM), energy dispersive X-ray spectroscopy (EDX), and X-ray diffraction (XRD) techniques. The Vickers-microhardness measurements, reciprocal wear, and electrochemical tests were conducted to evaluate the physical and anti-corrosion performance of the composite coatings. The findings indicate that the incorporation of Si_3N_4 nanoparticles not only changes the surface morphologies, compositions, and textures of the HEA matrix but also significantly enhances both the wear and anti-corrosion performance in artificial water by refining the microstructures and reducing the defects of the composite coatings. The HEA-3 g/L-Si_3N_4-40 mA/cm^2 and HEA-6 g/L-Si_3N_4-40 mA/cm^2 composite coatings demonstrate the best wear performance and anti-corrosion properties among the samples investigated, respectively. The present study shows a significant improvement in the mechanical and anti-corrosion properties of HEA coatings by incorporation of Si_3N_4 nanoparticles, which is a very promising approach for the surface protection of engineering materials used in corrosive and frictional-working conditions.

1. Introduction

The concept of multi-component alloys was first proposed by Franz Achard in 1788 [1] and was independently realized by Cantor [2] and Yeh's research teams [3] through melting and casting methods 20 years ago. They successfully prepared multi-component alloys and characterized their microstructures and properties. These alloys were named "high-entropy alloys" (HEAs) based on their thermodynamic characteristics, marking the onset of rapid development in this field. High-entropy alloys possess three distinct features: 1) Thermodynamic high-entropy effect [4], 2) Elemental sluggish diffusion effect from the kinetic aspect [5], and 3) Performance advantage of $1 + 1 > 2$ [6]. Compared to traditional metal alloys, high-entropy alloys demonstrate remarkable mechanical properties, such as high hardness [7], tensile strength [8], toughness [9], and plasticity [10]. As a result, they have garnered significant attention in recent years and found applications in various industries, including aerospace [11], nuclear power [12], and engineering [13]. Additionally, the concept and scope of high-entropy alloys have expanded greatly, encompassing not only multi-component metal alloys but also high-entropy ceramics [14], high-entropy oxides [15], and high-entropy compounds [16]. These high-entropy alloys are utilized not only in structural materials but also in catalysts [17], electromagnetic materials [18], and energy materials [19].

Initially, high-entropy alloys were prepared through melting and

* Corresponding author.
E-mail address: ningzhong@shmtu.edu.cn (N. Zhong).

https://doi.org/10.1016/j.jmrt.2024.09.262
Received 20 June 2024; Received in revised form 30 September 2024; Accepted 30 September 2024
Available online 1 October 2024

casting methods [2], and optimum microstructures and properties could be achieved through appropriate setting of plastic processing and heat treatment [20]. However, in production and engineering fields, failure often initiates from the surface due to the existence of mechanical, thermal, and corrosive interactions between the surface of mechanical parts and the surrounding environment [21]. Corrosion, wear, and the resulting formation of cracks and fractures are the primary failure forms of mechanical components [22,23]. Therefore, surface preparation and modification techniques, such as laser cladding [24], plasma spraying [25], flame spraying [26], electroplating [27], and magnetron sputtering [28], can be employed to deposit a layer of high-entropy alloy onto the substrate, achieving materials surface modification for enhanced properties. To utilize the chemical stability and excellent mechanical properties of high-entropy alloys, a high-entropy alloy coating can be produced on the surface of mechanical parts, effectively resisting corrosion in aggressive environments [29]. This, in turn, extends the service life of machinery, enhances production efficiency, and contributes to energy conservation and emission reduction. Compared to other surface-modification methods, such as laser cladding, plasma spraying, and magnetron sputtering, electroplating exhibits low equipment-requirements, simple and flexible operation, and allows for adjustment of composition and performance of high-entropy-alloy coatings by controlling processing parameters, such as temperature, current density, and pH value [30–33]. Currently, researchers have successfully deposited various series of medium-entropy alloy and high-entropy alloy systems from aqueous or organic solvents using electroplating methods [34,35]. For example, Pavithra et al. utilized pulse electrodeposition to fabricate Co–Cu–Fe–Ni–Zn nanocrystalline dual-phase high-entropy alloy films, which demonstrated superior corrosion and oxidation resistance, compared to traditional magnetic materials [36]. Nagy et al. achieved uniform Co–Fe–Ni–Zn high-entropy alloy coatings through pulse electrodeposition, showing exceptionally high hardness and elastic modulus attributed to the small grain size and a reasonable proportion of amorphous phases [37]. The deposition of the CoFeNiMoW-HEA films by direct current electrodeposition conducted by Freitas et al. [38] demonstrated the simplicity and feasibility of electroplating techniques in producing various high-entropy alloys. Through 57-Fe Conversion Electron Mössbauer Spectroscopy (CEM) [38] experiments, they verified the chemical disorder of the Fe element and the absence of oxides/hydroxides in the film structure. Haché et al. synthesized NiFeCo–W, NiFeCoMo, and NiFeCo–MoW high-entropy alloys, which exhibited higher hardness due to their unique nanocrystalline-amorphous structures, revealing the reasons behind their hardness and hardness-to-density ratio [27]. Bian et al. simplified the electrodeposition process to synthesize nanoporous NFCCW-HEA electrocatalysts, demonstrating excellent catalytic-reaction kinetics and stability owing to their distinctive surface structures, low overpotential, and smaller Tafel slopes [39]. Although considerable research and publications in the field of electroplating for high-entropy alloy synthesis have been conducted, most of these studies have focused on the synthesis and microstructure characterization of high-entropy alloys, with only a few providing systematic exploration of electroplating processes, structures, and physical properties [27]. Currently, there is hardly any literature reporting the preparation of ceramic particle-reinforced high-entropy alloy composites using electroplating techniques to the best of our knowledge [40].

Ceramic-reinforced metal-matrix composites combine the advantages of ceramics, such as high strength, hardness, wear resistance, with the good plasticity, toughness, and processability of matrix metals [41,42]. They are widely utilized in aerospace, automotive, and chemical industries because these composites not only possess high strength and hardness but also exhibit good plasticity, toughness, and improved resistance to brittle fracture, thereby enhancing the safety and reliability of components [43]. However, traditional methods for fabricating ceramic-reinforced metal matrix composites are complex and costly, requiring significant equipment investments, such as powder metallurgy and spray deposition. On the other hand, electroplating has proven to be an effective method for producing metal-matrix composites [44,45]. However, there are currently very few reports on electroplating for the preparation of high-entropy alloy composites, with only graphene oxides (GO) [46,47] and carbon nanotubes [48] (CNT)-reinforced high-entropy alloy composites being reported. Nevertheless, both GO and CNTs are expensive materials, limiting the widespread application of these composites. Ceramic particles, such as Si_3N_4, are relatively inexpensive and possess high hardness, thermal conductivity, excellent thermal stability, and chemical stability [49]. Therefore, Si_3N_4 was chosen as the reinforcing phase in this study for high-entropy alloy systems. In the current research, a direct current electroplating technique was employed to deposit Si_3N_4-reinforced high-entropy alloy nanocomposite coatings on AISI4140 steel substrates. Here, NiCoFeCu is selected as an HEA matrix [33], and the Cr element is excluded from the alloy component, because during the electro-crystallization process on the cathode surface, the hexagonal chromium hydride (CrH_x) is usually formed [50], which would lead to high inner stresses and cracking of coatings. Besides, the electrodeposition from the Cr-ions-free solution shows attractive prospects for environmental friendliness without Cr^{6+}.

In this study, Si_3N_4-reinforced HEA nanocomposite coatings were deposited by a direct current method [45]. with varying loadings of Si_3N_4 nanoparticles in the electrolyte bath, focusing on studying the effects of Si_3N_4 contents and the current density on the morphologies, microstructures, hardness, and tribological properties of Si_3N_4-reinforced NiCoFeCu HEA composite coatings. The present study aims to investigate the enhancement mechanism of Si_3N_4-reinforced NiCoFeCu composite coatings with the objective of offering potential engineering applications of HEA-composite coatings under corrosive and friction conditions.

2. Materials and methods

2.1. Materials

Table 1 provides the detailed information about electrolytes. All the chemicals used were of an analytical grade and sourced from Sinopharm Chemical Reagent Co., Ltd. (Shanghai, China). The electrolyte contained boric acid as a buffering agent, sodium dodecyl sulfate (SDS) as a wetting agent, and sodium citrate as a complexing agent. The Si_3N_4 particles were purchased from the Shanghai ST-NANO Science & Technology Co., Ltd., and the morphology and phase constitute are shown in Fig. 1 (a) and 1 (b), demonstrating the primary hexagonal phase with the average grain size of 50 nm, respectively. The aqueous electrolyte was prepared using the deionized water by adding the chemicals in a special order and time interval under continual stirring for the purpose to avoid precipitation of oxides/hydra oxides [33]. The temperature was set to 35 °C, and the pH was adjusted to 4.8 with dilute sulfuric acid. Current densities ranging from 20 to 60 mA/cm^2 were selected to analyze their

Table 1
Electrolyte composition and electro-co-deposition conditions.

Bath ingredients	NiCoFeCu–Si_3N_4 composites
Nickel sulfate·6H_2O(g/L)	118.28
Cobalt sulfate·6H_2O(g/L)	12.64
Ferrous sulfate·7H_2O(g/L)	8.34
Cupric sulfate·5H_2O(g/L)	3.74
Boric acid(g/L)	29.66
Saccharin (g/L)	2.0
Trisodium Citrate(g/L)	41.17
Loadings of Si_3N_4(g/L)	3, 6, 10
Current density (mA/cm^2)	20, 40, 60
pH	4.5
Time (minutes)	70
Agitation (rpm)	280
Temperature (°C)	35

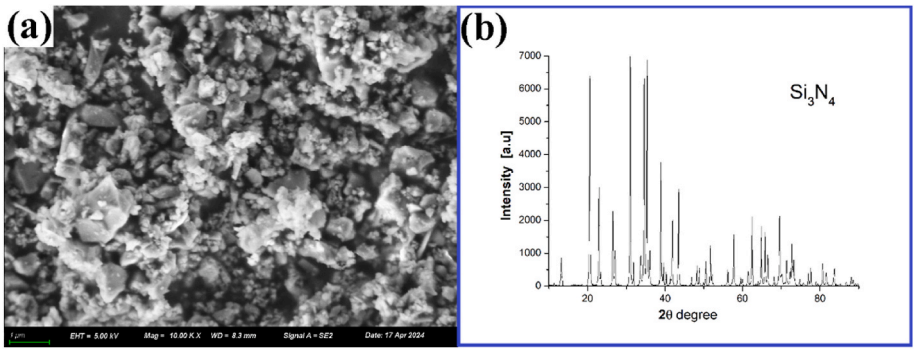

Fig. 1. The morphology (a) and phase constitute (b) of Si_3N_4 particles.

impact on the microstructures and properties of the composite coatings. Substrate materials were pure copper sheets (20.0 mm × 10.0 mm × 1.0 mm) and high strength low carbon steel (HSLA) (10.0 mm × 10.0 mm × 1.0 mm) for wear tests and electrochemical performance, respectively. To achieve a mirror surface condition for electrodeposition, the substrates were polished with silicon carbide papers in the order of 400 #, 800 #, 1000 #, and 1500 # grade, followed by washed and cleaned with acetone. Before electrodeposition, the substrates were etched in a 12 wt % hydrochloric acid solution. An auxiliary anode in the form of a graphite electrode (40 mm × 40 mm) was utilized, and the working space between the graphite electrode and the substrates was 20 mm. The deposited time was 45 min for each specimen. When it was finished, the specimen was taken out and ultrasonically washed in the distilled water for about 10 s to remove the attached ceramic particles on the surface, and then dried in an oven. For simplicity, for example, "NiCoFeCu-3 g/L-Si_3N_4-20 mA/cm^2", deposited with 3 g/L Si_3N_4 loading in the electrolyte at a current density of 20 mA/cm^2, is abbreviated to "HEA-3 g/L-20 mA".

2.2. Microstructural characterization

The phase constitutes of the HEA composite coatings were determined using an X-ray diffraction technique with Cu K_α radiation (λ = 1.5405 Å) on a RIGAKU SmartLab [33], operating at a voltage of 30 kV and a beam current of 30 mA. The diffraction patterns of the specimens were obtained in the angle range of 30°–100° at the scan rate of 6°/min., and the grain sizes of the different HEA composite coatings were estimated using the Scherrer equation [51].

$$D = k\lambda/\beta \cos\theta \quad (1)$$

where D represents the average grain size of the coatings in nm, k is the Scherrer constant (0.94), λ denotes the K_α wavelength of copper (~0.15405 nm), and β is the peak width at a half maximum of the diffraction angle in radian.

The relative texture coefficients (RTC) for different HEA composite coatings were computed by the formula [44]:

$$RTC(hkl) = \frac{I(hkl)/I_0(hkl)}{\sum I(hkl)/I_0(hkl)} \quad (2)$$

where I_0 (h k l) is the intensity of an untextured nickel sample (JCPDF No. 04–0850), and I (h k l) is the diffraction intensity of the (h k l) reflection.

A JOEL-7500F scanning electron microscope (SEM) was used for the observation of the surface morphologies of the HEA coatings. The compositions of the HEA coatings were estimated by an Oxford Energy Dispersive X-ray Spectrometer (EDS) attached to the SEM.

The sample surface roughness (Ra) was measured using a Roughness and Contour Meter (manufactured by Shanghai Taile Ltd.), with five areas measured for each sample and the average value taken.2.3 Electrochemical measurements.

The electrochemical measurements were performed at room temperature using a CHI 660e workstation. A three-electrode setup was employed in a glass cell with a 350 mL 3.5 wt% sodium chloride solution for the electrochemical measurements of the HEA composite coatings. The counter and reference electrodes were a platinum plate and a saturated calomel electrode (SCE), respectively. Therefore, the potentials mentioned in the work were referenced to SCE. Potentiodynamic polarization and electrochemical impedance spectroscopy (EIS) measurements were performed in a solution at 25 °C. The specimens were soaked in the chloride solution for 45 min or longer until they reached a stable open circuit potential (E_{ocp}) before the electrochemical measurements. The polarization tests were measured in the potential range of ±250 mV with respect to the E_{ocp} with a potential scanning speed of 1 mV/s, while the EIS data was recorded applying a frequency range of 0.01 Hz–100 kHz with an amplitude of 10 mV. The corrosion-current density for the HEA composite coatings was determined using the Tafel extrapolation method [52], and the analysis of parameters for the corresponding electrical equivalent circuit (EEC) was carried out using the ZVIEW software [53].

2.3. Measurement of hardness and wear performance

The microhardness values were measured using an Mh-VK hardness tester and a Vickers hardness indenter, with a loading force of 50 g and a dwell time of 15 s. Microhardness measurements were taken at five different locations, leading to the average values of microhardness. Reciprocating wear tests were conducted using a BRUKER UMT Tribo-Lab (Germany), with a frequency of 4 Hz and a stroke length of 5 mm. This process was performed against an Al_2O_3 ball with a diameter of 8 mm and a hardness of 1600 HV. A loading force of 9.8 N was applied to the sample surface for 10 min. The wear tests were carried out in ambient air at room temperature and humidity. The surface characteristics of composite coatings were examined by a surface profiler (Contour GT, Bruker, Germany).

3. Results

3.1. Surface morphologies and microstructures of Si_3N_4-reinforced NiCoFeCu composite coatings under varying current densities and Si_3N_4 loadings

The surface morphologies of Si_3N_4-reinforced NiCoFeCu composite coatings deposited at 40 mA/cm^2 are depicted in Fig. 2, where the insets are the corresponding high magnification images. Compared to pristine NiCoFeCu coatings without the addition of Si_3N_4, the Si_3N_4-reinforced NiCoFeCu composite coatings reveal a rather rough and uneven surface, characterized by globular structures, as shown in Fig. 2 (b, c, d). No noticeable defects, such as cracks, pores, or pinholes, were found in any of the samples. The insert magnified images in Fig. 2 (c, d) reveal that

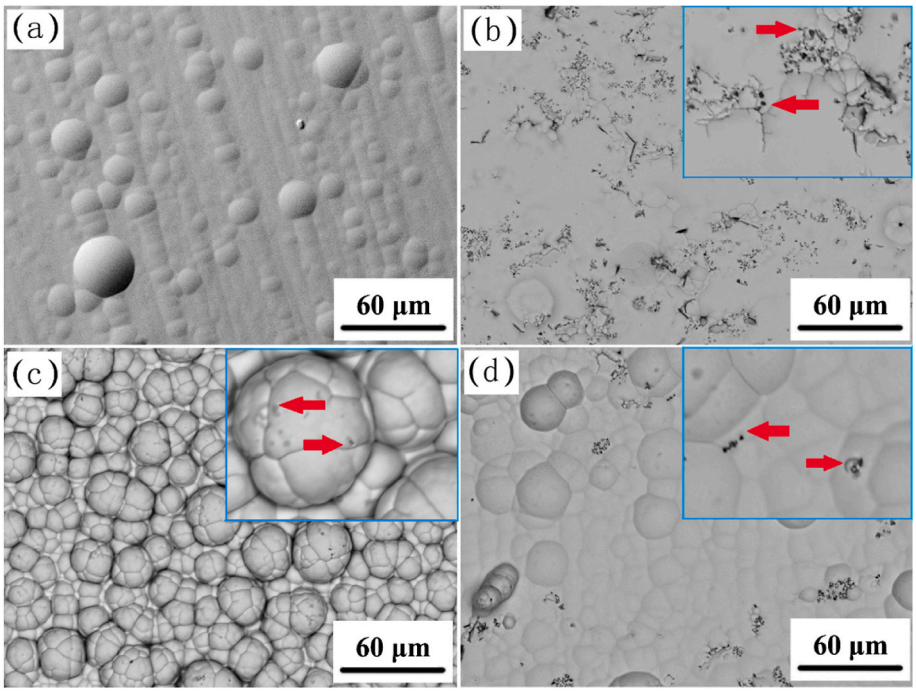

Fig. 2. SEM micrographs of composite coatings deposited at current densities of 40 mA/cm^2 and Si_3N_4 loading of 0 g/L (a), 3 g/L (b), 6 g/L (c), and 10 g/L (d) in the electrolyte.

the Si_3N_4 nanoparticles are nearly spherical with a dark contrast, as indicated by the arrows. Furthermore, SEM observations indicate that the surface morphology becomes increasingly uneven as the loading of Si_3N_4 increases to 10 g/L.

The surface characteristics of HEA-6 g/L composite coatings deposited at different current densities are shown in Fig. 3. As the current density increases, the surface roughness of the HEA composite coatings also increases. At the current density of 40 mA/cm^2, the average size of the nodular structures is approximately 15 μm, and when the current density reaches 60 mA/cm^2, the dimensions of the nodular structures on the surface appears to be non-uniform, with some large-sized particles reaching up to 40 μm. Additionally, it's noted that most Si_3N_4 particles are embedded at the top of the large nodular structures, as shown in Fig. 3(d). Fig. 4 illustrates the average roughness values of HEA composite coatings deposited at various current densities. In general, the average roughness of the composite coatings exhibits a slight increase in response to higher current densities. This trend could be attributed to the intensified local electric field, which influences the deposition and

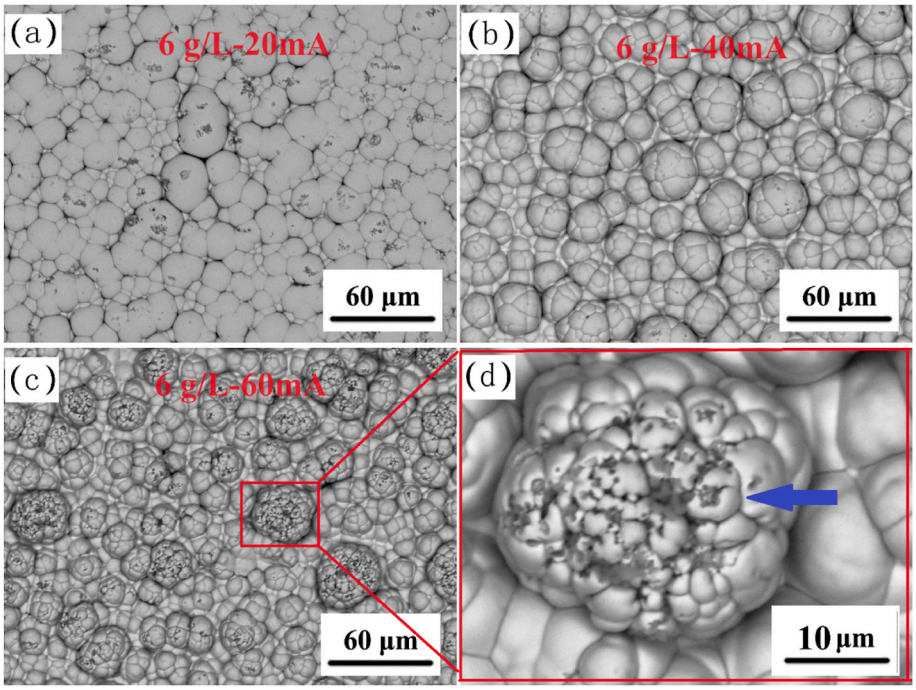

Fig. 3. Surface morphologies of HEA composite coatings electrodeposited with 20 mA/cm^2 (a), 40 mA/cm^2 (b), and 60 mA/cm^2 (c, d) in an electrolyte with a Si_3N_4 loading of 6 g/L.

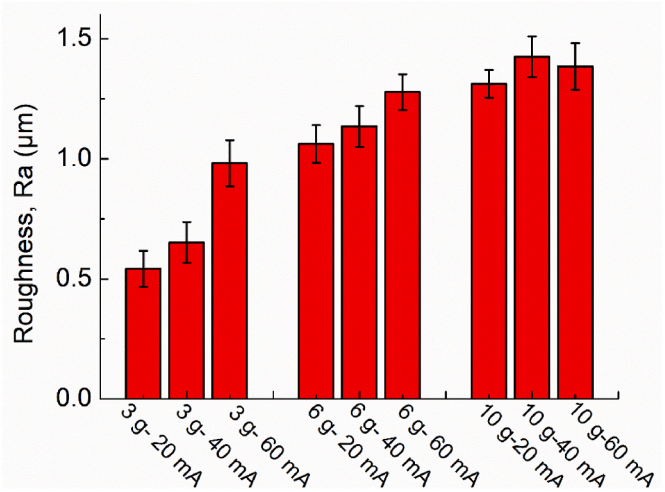

Fig. 4. The average surface roughness of the samples varies with different electroplating current densities and Si_3N_4 particle concentrations.

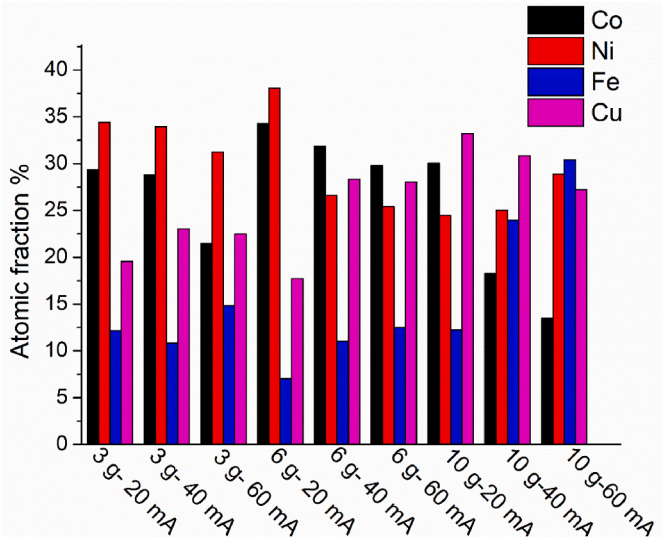

Fig. 6. The elemental contents of NiCoFeCu–Si_3N_4-composite coatings.

crystallization rates of the HEA grains, resulting in a rougher surface texture [54].

The EDS mappings of composite coatings in Fig. 5 show the homogeneous distributions of Fe, Co, and Cu elements. However, the agglomerations of Si and N element are visible due to the inhomogeneous distribution of Si_3N_4 nanoparticles. The chemical compositions of Si_3N_4-reinforced NiCoFeCu HEA alloys are shown in Fig. 6, displaying the four elements of Ni, Co, Fe, and Cu, which indicates the successful co-deposition for producing a uniform high-entropy alloy coating.

Fig. 7 displays the cross-sectional images of the HEA-6 g/L-40 mA and HEA-10 g/L-40 mA coatings, demonstrating the average thicknesses of approximately 45 μm and 42 μm, respectively. The samples exhibit cohesive, crack-free layers with good adhesion to the copper substrates. The EDS line scans in Fig. 7 (c, d) reveal relatively uniform distributions of Ni, Co, and Fe elements, whereas Si and N elements exhibit notable compositional variations along the distance, confirming that the incorporation of Si_3N_4 particles into the HEA matrix.

3.2. Phase constitutes

The XRD patterns in Fig. 8 show that all the composite coatings display a typical face-centered-cubic (FCC) structure, except for the ones deposited at 60 mA/cm^2. The characteristic peaks with diffraction angles of approximately 44.5°, 51.9°, 76.5°, 93.1°, and 98.5°, respectively, are associated with the (1 1 1), (2 0 0), (2 2 0), (3 1 1), and (2 2 2) planes of an FCC solid solution (PDF card No. 04–0850).

3.3. Hardness

The microhardness values of the composite coatings are presented in Fig. 9. The NiCoFeCu deposit shows the lowest value of 630 HV_{50g}, and the hardness values of Si_3N_4-reinforced NiCoFeCu composite coatings increase obviously with the addition of Si_3N_4. However, it seems that increasing the loadings of Si_3N_4 has a little effect on the microhardness of the composite coatings in the deposition current density range of 20–60 mA/cm^2, and because of the roughness of the surface, the hardness values are more widely distributed especially for the samples deposited with high loadings of ceramic particles at high current densities.

3.4. Tribological performance

Composite coatings deposited without the Si_3N_4 addition to the electrolyte solution exhibit relatively stable friction coefficients during reciprocating sliding tests at ambient temperature, hovering around the value of 0.5, as illustrated in Fig. 10. Upon the addition of Si_3N_4, there is a slight decrease in the friction coefficient of the composite coatings, and only a minor difference is observed between the composite coatings deposited from the electrolyte solution containing 3 g/L and 6 g/L of Si_3N_4. However, when the amount of Si_3N_4 loading reaches 10 g/L, the friction coefficients of the samples significantly rise. Particularly, the sample deposited at a current density of 60 mA/cm^2 shows the highest value of a friction coefficient, averaging around 0.9, and displays a noticeable fluctuation in the CoF value during the reciprocating sliding test.

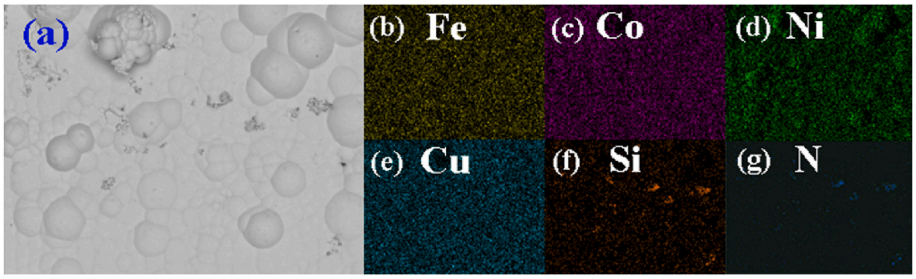

Fig. 5. SEM micrograph of the FCCN-6 g/L-20mA sample deposited with 40 mA/cm^2 for 45 min. (a) and the corresponding EDS mapping of Fe, Co, Cu, Ni, N and Si elements, respectively (b, c, d, e).

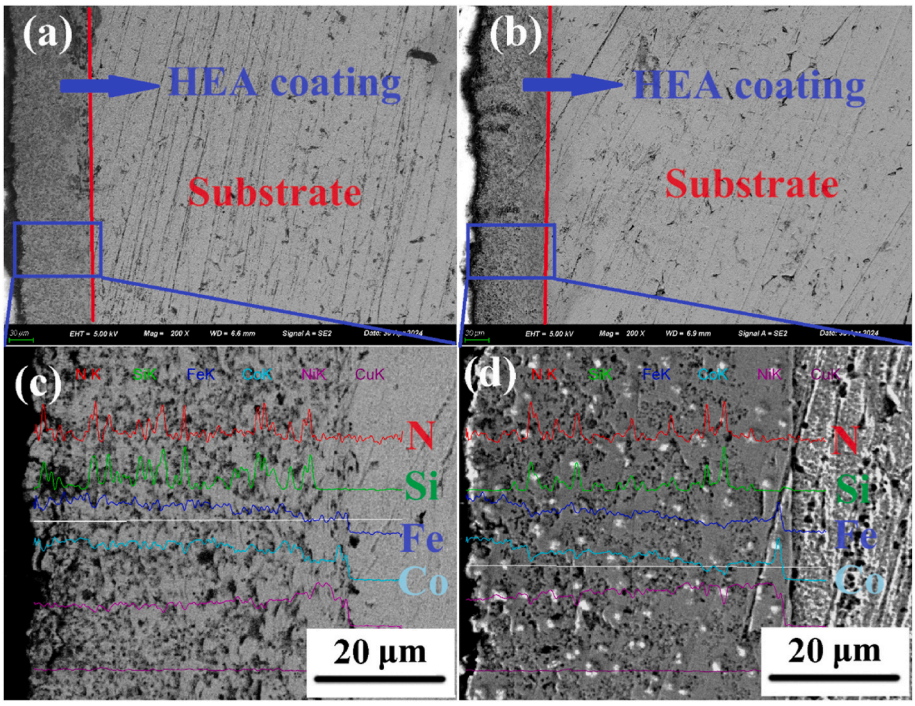

Fig. 7. Cross-sectional images of the HEA-6 g/L-40 mA (a, c) and HEA-10 g/L-40 mA coatings (b, d).

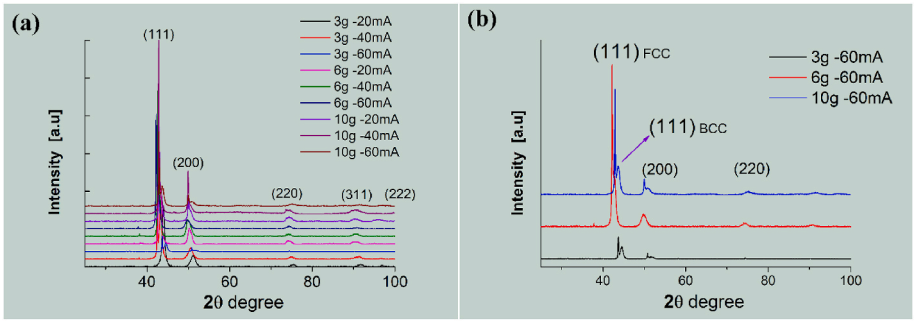

Fig. 8. XRD patterns of the composite coatings deposited under various current densities (20, 40, and 60 mA/cm^2) and Si_3N_4 loadings (3, 6, and 10 g/L) for 70 min.

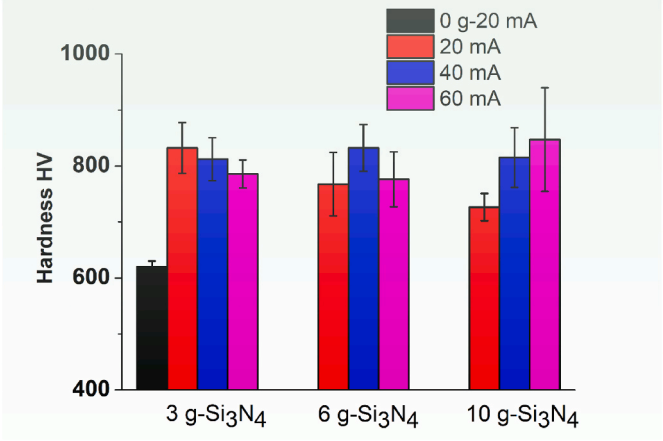

Fig. 9. Hardness values of the composite coatings deposited under different current densities and Si_3N_4 loadings for 70 min.

4. Discussion

4.1. *Effect of Si_3N_4 loadings and current densities on the surface morphologies and microstructures of NiCoFeCu composite coatings*

As the loadings of Si_3N_4 particles increase, the surface morphologies of NiCoFeCu composite coatings become rougher and less uniform (Figs. 2 and 3). This phenomenon arises from the coupled process of the electrochemical reduction of metal ions on the cathode surface and the co-deposition of Si_3N_4 particles in the electrolyte under the force of the electric field. Typically, ceramic particles with good conductivity in the electrolyte attract a large amount of charged ions to their surfaces. With the effects of stirring and convection, corresponding mass transfer processes occurred in the electrolyte solution. After the charged Si_3N_4 particles reached the double layer of the cathode, they could embed themselves into the growing front of the deposit layer along with the metal-cations reduction, thus forming the ceramic-particle-reinforced HEA composite materials. This process can be described using a Guglielmi's model [55], as shown in Fig. 11. There are two key steps in this co-deposition process: namely the "weak adsorption" of ceramic particles on the cathode surface and the "strong adsorption" generated as metal cations on the ceramic particles were electrochemically reduced

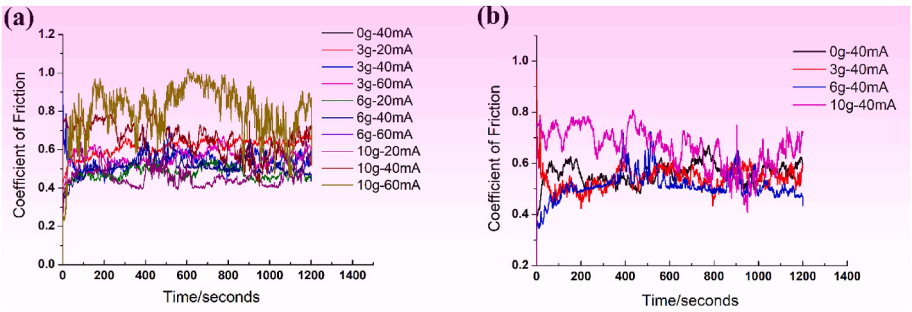

Fig. 10. The coefficients of friction (CoF) of the composite coatings acquired with an Al_2O_3 counter ball at an ambient temperature of 25 °C.

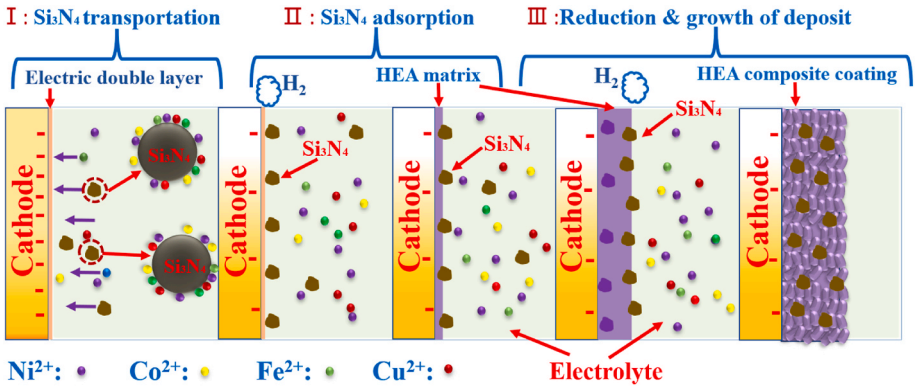

Fig. 11. The schematic diagram shows the co-deposition process of Si_3N_4 nanoparticles in the electrolyte bath containing Fe, Co, Ni, and Cu cations.

with particle embedding. Additionally, by adding Si_3N_4 particles to the HEA electrolyte, the electric-field distribution at the growth front varied and could provide more nucleation sites for crystallization. While promoting the refinement of the coatings' microstructures, it simultaneously led to an uneven cation transfer on the surface and localized grain growth. Consequently, with an increase in the particle concentration, the surface roughness also increases. This experimental observation aligns with the Ni–P–SiC composite coatings, as reported by Zhang et al. [56]. What' more, the inclusion of ceramic particles also helps in reducing or even eliminating the formation of pinholes and gas pores during the electroplating process, resulting in a denser coating and uniform microstructures [45].

The current density is one of the crucial operational parameters of electrodeposition. With an increase in the current density, the rate of the electrochemical reduction of metal cations also increases. Consequently, local regions at the cathode-growing front are more likely to exhibit an uneven electric field distribution and an enhanced degree of ionic-concentration polarization, leading to an increased surface roughness of the deposition layer, as exhibited in Fig. 3. Additionally, as the deposition current density increases, the size disparity between the nodular and coronal grains becomes more pronounced, resulting in the increased surface roughness and inhomogeneity of the coatings. Moreover, in the composite coating deposited with the maximum current density, distinctive cauliflower-like structures composed of many small grains appear, as indicated by the arrows in Fig. 3(c and d). The phenomenon can be attributed to the aggregation of ceramic particles [57], and the similar nodular morphology is similar to the previous report [58].

The chemical compositions of the composite coatings were determined through the energy dispersive X-ray spectroscopy (EDS), with results presented in Fig. 6. Despite the significant differences in the standard reduction potentials of the four elements (Fe = 0.44 V, Co = 0.28 V, Ni = 0.25 V, and Cu = 0.34 V), the EDS analysis indicates the successful co-deposition of these elements in the composite coatings. According to the definition of HEAs [59], the elemental content typically ranges between 5% and 35%, suggesting that the composite coatings prepared in the present study meet the criteria of HEAs. Additionally, the contents of Fe increase while the contents of Co show a decreasing trend with the increase in applied deposition current density. This can be attributed to the anomalous co-deposition of Fe and Co, similar results have also been reported in the literature [45]. In comparison, the contents of Ni and Cu of the samples derived from different conditions exhibit no significant changes with the increase in current density. Besides, when the concentration of Si_3N_4 in the electrolyte is increased, particularly when the concentration reaches 10 g/L, there is a significant increase in the Fe element in the electrodeposited coating. This may be due to the adsorption and interaction of Fe ions in the electrolyte with the surface of Si_3N_4 particles [60]. Finally, it is noteworthy that the results reveal no specific trend in the elemental content with an increase in ceramic loadings in the electrolyte in this study. Further research is needed to investigate this phenomenon.

4.2. *Effect of current densities and Si_3N_4 loadings on phase constitutes of Si_3N_4-reinforced NiCoFeCu composite coatings*

The XRD analysis reveals that the primary phase constitute is the FCC phase (Fig. 8), which is consistent with the previous research [38]. However, the diffraction peaks, related to the Si_3N_4 phase, were very weak and difficult to detect due to the very small number of Si_3N_4-particles incorporated into the HEA matrix. Additionally, when the deposition current density reached 60 mA/cm^2, the BCC (Body-Centered Cubic) phase began to appear, as illustrated in Fig. 8(b). The peaks, characterized as the BCC phase, appeared near 45° and were highlighted by the arrows. Generally, in HEA alloys containing Cr and Fe elements, both of which are stabilizing elements of the BCC phase, the HEA alloys tend to form the low-energy BCC phase enriched with Fe and Ni. In the present alloy system, since it contains only the Fe element (Cu and Ni are the elements that stabilize the FCC phase), only a single FCC phase

structure is detected at small deposition current densities (20–40 mA/cm^2). As the deposition current density increases to 60 mA/cm^2, there is a significant increase in the Fe content of the HEA coatings. Therefore, the deposit tends to be made up of a mix phase structure containing the BCC phase to thermodynamically reduce the overall Gibbs free energy [61]. Generally, the presence of a duplex structure in material microstructure could deteriorate its corrosion resistance due to the formation of galvanic corrosion cells under corrosive environment. The grain sizes and relative texture coefficients (RTC) of the composite deposits were determined through the XRD analysis, and the results are summarized in Table 2 (the calculations were based only on the diffraction data of the FCC phases). Compared to the pristine HEA coatings without the Si_3N_4 addition, the grain size of the composite coatings slightly decreased with the addition of Si_3N_4 particles (3 g/L). This observed phenomenon aligns with the general rule in ceramic-reinforced composite materials. The introduction of the reinforcing phase can create more nucleation sites during the electrodeposition, leading to grain refinement for the composite coatings. Additionally, according to the following formula [62]:

$$A = K_1 \exp\left(\frac{-\Delta G^*}{k_B T}\right) = K_1 \exp\left(\frac{K_2}{\eta^2}\right) \quad (3)$$

where K_1 and K_2 are the constants under certain conditions, ΔG^* is the Gibbs energy of nucleation, η is the nucleation overpotential (positively correlated to the deposition current density), k_B is the Boltzmann constant, and T is the absolute temperature.

Therefore, increasing the deposition current density (overpotential), can obviously enhance nucleation rates, further refining the microstructures. However, as the reinforcement phase concentration increases beyond a loading of 6 g/L, the grain size of the HEA composites no longer decreases but inversely increases slowly, as shown in Table 2. When the reinforcing phase concentration reaches 10 g/L, the grain size of the composite coatings can exceed 30 nm, presenting an increase of 20%, compared to that deposited from the 3 g/L electrolyte. The reason for this increase might be related to the agglomeration of the Si_3N_4 particles [62], which requires further investigation.

The addition of Si_3N_4 particles also altered the crystal texture of the composite coatings. As the concentration of the particles increases, the texture of the (3 1 1) crystal plane gradually weakened, while the (1 1 1) and (2 0 0) crystal planes became preferred orientations in the composite coatings, especially prominent when deposited with high particle concentrations and current densities. The textures of the (2 0 0) and (1 1 1) planes of the composite coatings favors enhanced anti-corrosion resistance due to their characteristic low-energy surfaces [63].

Table 2
The grain size and relative texture coefficients (RTC) of the nanocomposite coatings.

Samples	Grain size (111) plane	Grain size (200) plane	RTC_{111}	RTC_{200}	RTC_{220}	RTC_{311}
0g-40 mA	19.2	15.6	0.521	0.134	0.069	0.104
3g-20 mA	18.9	15.5	0.504	0.191	0.098	0.078
3g-40 mA	18.2	16.4	0.501	0.175	0.083	0.082
3g-60 mA	17.9	17.2	0.532	0.184	0.081	0.075
6g-20 mA	16.8	15.4	0.452	0.242	0.125	0.081
6g-40 mA	19.5	16.4	0.662	0.251	0.061	0.043
6g-60 mA	20.8	17.2	0.621	0.182	0.084	0.052
10g-20 mA	25.9	18.2	0.536	0.261	0.089	0.029
10g-40 mA	28.8	21.9	0.625	0.305	0.048	0.022
10g-60 mA	19.6	20.1	0.614	0.241	0.064	0.025

4.3. Wear performance of HEA composites

Fig. 10 shows the coefficients of friction (CoF) of the samples recorded under dry sliding wear conditions at an ambient temperature of 25 °C. The results indicate that as the loadings of ceramic particles increase, the values of CoF of composite coatings show a slight decrease, followed by a gradual rise. When the Si_3N_4 loading is 3 g/L, the obtained composite coatings exhibit slightly lower CoF values than that of the pristine HEA coating within the deposition current density range of 20–60 mA/cm^2. This phenomenon is attributed to the Si_3N_4 particles acting as solid lubricants during reciprocating friction, reducing the values of CoF between the friction pair and the composite coatings [64]. However, with a further increase in ceramic loading, particularly in the composite coatings deposited at high current densities, the surface roughness and unevenness noticeably increase, which leads to not only an increase in the CoF values but also distinct fluctuations in the friction curve, as detailed in Fig. 10(b). Specifically, for samples deposited at current densities of 40 and 60 mA/cm^2 and with a ceramic particle loading of 10 g/L, the value of CoF can exceed 0.9, which could be attributed to the unevenness in the surface structure. Generally, an increase in the surface roughness of samples tends to increase in the coefficient of friction during dry sliding. Sajjadnejad et al. [60] have demonstrated that incorporating Si_3N_4 particles into a pure Ni matrix via electroplating could increase the coefficient of friction, and their findings are similar to the present results.

The white-light interferometric images of samples obtained at a deposition current density of 40 mA/cm^2 after wear tests are shown in Fig. 12. Compared with a pristine HEA coating, the addition of Si_3N_4 particles significantly reduces the wear volume of the composite coatings. The coating prepared with a Si_3N_4 loading of 3 g/L exhibits the smallest wear volume, followed by the sample obtained with a Si_3N_4 loading of 6 g/L, while the coating prepared with a ceramic loading of 10 g/L shows a noticeable increase in the wear volume. The results from white-light interferometry indicate that the wear volume increases with the loading of ceramic particles in the electrolyte solution, implying that a higher content of Si_3N_4 particles does not necessarily lead to better wear performances. The possible reasons for this phenomenon include: (1). Composite coatings obtained from plating solutions with high Si_3N_4 concentrations exhibit more uneven surface morphologies. (2). According to Archard's principle, there is an inverse relationship between the resistance to frictional wear and the hardness of the coatings [65].

$$V = kWL/H \quad (4)$$

where V is the wear volume, k denotes the wear coefficient (dimensionless constant), W is normal loading, L represents the sliding distance, and H is the hardness of the contacting surfaces.

Based on the grain size obtained from the XRD tests, when the Si_3N_4 particle loading reaches 10 g/L in the electrolyte, the grain sizes of the composite coatings gradually increase compared to those obtained at 6 g/L loading, and the hardness gradually decreases, leading to relatively reduced wear resistance and an increase in wear volume for the HEA-10 g/L coatings.

The worn surfaces of the composite coatings were examined using SEM, with the results displayed in Fig. 13. The wear tracks of all the composite coatings exhibit abrasive grooves and debris with different sizes, indicating a wear mechanism governed by a combination of adhesive and abrasive wear. The worn surface of the HEA-3 g/L-40 mA displays the smallest wear-track width and depth, indicating superior wear resistance. The incorporation of Si_3N_4 nanoparticles into the HEA coatings enhances the wear resistance, attributed to both grain-size refinement and the dispersion-strengthening effect, compared to pristine HEA coatings [58]. Besides, the uniform and compact morphology

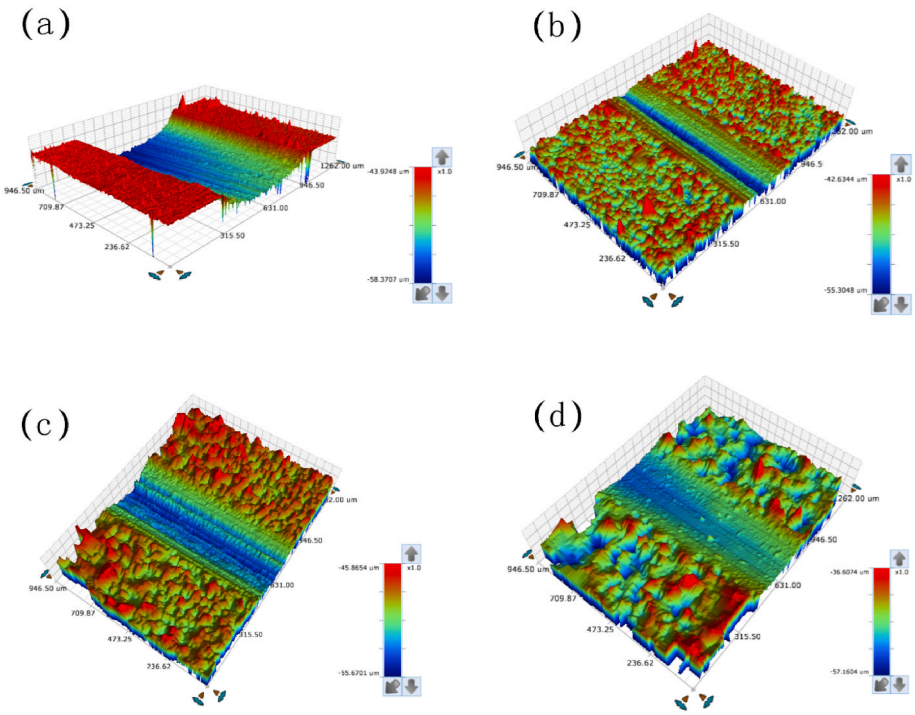

Fig. 12. White-light interferometric images of samples prepared under a deposition current density of 40 mA/cm^2 with varying loadings of Si_3N_4 after wear tests. 0 g/L (a), 3 g/L (b), 6 g/L (c), and 10 g/L (d).

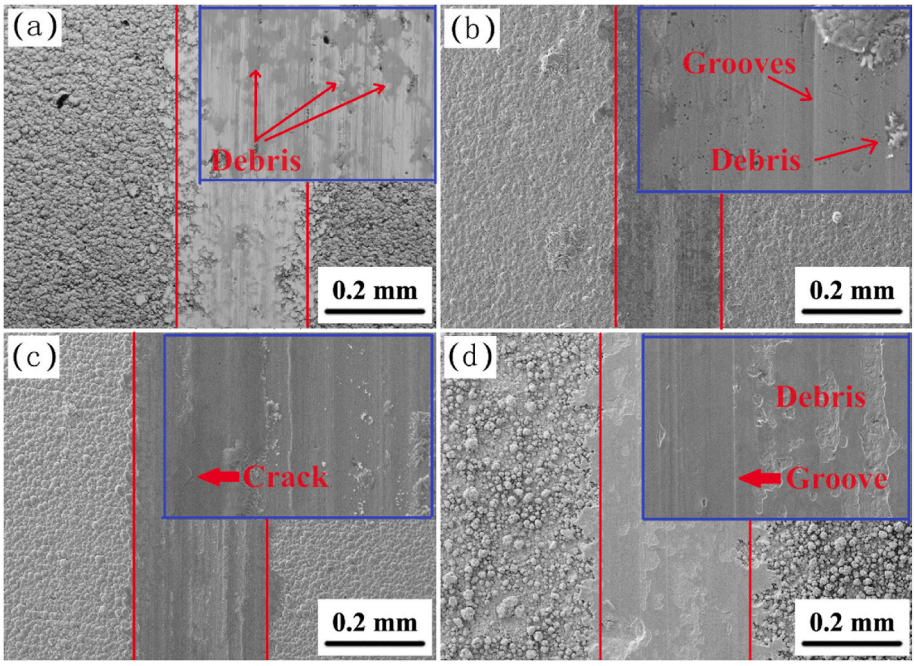

Fig. 13. SEM micrographs of the worn surface for the composite coatings deposited at a current density of 40 mA/cm^2 containing different Si_3N_4 loadings: 0 g/L (a), 3 g/L (b), 6 g/L (c), and 10 g/L (d).

of the HEA-3 g/L-40 mA sample is responsible for its good anti-wear resistance. It is worth noting that an increase in Si_3N_4 loading up to 10 g/L leads to heightened surface roughness. This increase in surface roughness contributes to an elevated wear rate and weight loss during the reciprocal-sliding process, as well as the values of CoF. Similar results have been reported in TiB_2/Al composites by Chi et al. [66]. Additionally, the agglomeration of Si_3N_4 nanoparticles could lead to the increased grain size and reduced hardness, potentially resulting in a greater wear volume loss compared to other composite coatings, as evidenced in Fig. 13 (d).

4.4. Corrosion properties of the HEA composite coatings

Fig. 14 displays the results of the polarization testing of the composite coatings in a 3.5 wt percent sodium chloride solution. The electrochemical parameters, including the corrosion current density (i_{corr}),

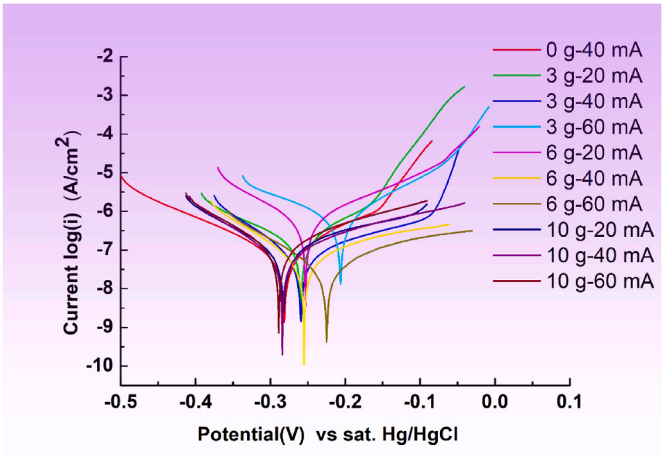

Fig. 14. Polarization curves for the HEA composite coatings in the 3.5 wt% NaCl (25 °C, 1 mV/s).

open circuit potential (E_{corr}), and Tafel slopes (β_α and β_c), related to corrosion resistance were determined using the Tafel extrapolation method [52]. It is known that the i_{corr} value could reflect the corrosion rate and durability of the coatings in a specific corrosive environment. Compared to the HEA coatings without the Si_3N_4 addition, the composite coatings prepared by electrodeposition with Si_3N_4 nanoparticles at appropriate current densities showed a significant decrease in the corrosion current density, as observed in samples like HEA-3 g/L-40 mA and HEA-6 g/L-40 mA, indicating an obvious enhancement in corrosion resistance. Among these samples, HEA-6 g/L-40 mA exhibited the lowest i_{corr} value and a relatively higher E_{corr} value, suggesting that it's the most corrosion-resistant coating among all samples tested. It should be noted that the coupled effect of the deposition-current density and ceramic incorporation significantly influences the microstructures and corrosion resistance of the composite coatings. For instance, in the HEA-10 g/L samples prepared at current densities between 20 and 60 mA, the corrosion current densities obtained from the Tafel curves were obviously higher than those of the original HEA coating, possibly due to the aggregation of Si_3N_4 particles and the uneven microstructure on the surface of these coatings [57].

Fig. 15 presents the results of electrochemical-impedance spectroscopy (EIS) conducted on the composite coatings immersed in a 3.5 wt% NaCl solution at a stable open circuit potential, with a testing frequency range of 0.01 Hz–100 kHz. The Nyquist plots of each coating revealed flattened circular arcs of different radii, where the arc sizes could

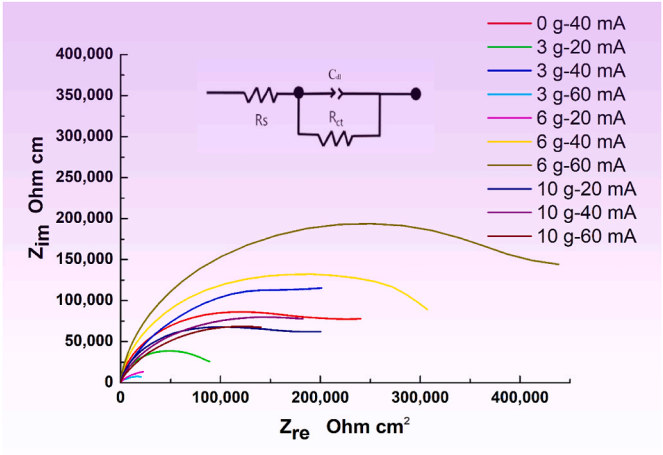

Fig. 15. Nyquist plots for the HEA composite coatings in the 3.5 wt% NaCl at an open circuit potential and the equivalent circuit (insert).

roughly correspond to the impedance values of the composite coatings. Notably, the impedance arc sizes for HEA-6 g/L-40 mA and HEA-6 g/L-60 mA were significantly larger than those of other coatings, indicating superior corrosion resistance compared to other samples. The EIS results were consistent with the previous Tafel polarization study.

To further explore the corrosion mechanism of the composite coatings, the EIS data were fitted using an electrical equivalent circuit (EEC). Two-time constants, reflecting two double-layer capacitors, were considered in the fitting based on the characteristics of the impedance spectra. The EEC model included the charge transfer resistance (R_{ct}), coating resistance (R_{coat}), and solution resistance (R_s). Due to the dispersive effects of the capacitive loop, a constant phase element (CPE) was used in the CCE instead of the ideal capacitor. The CPE impedance can be described as follows,

$$Z_{CPE} = Y_0^{-1}(j\omega)^{-n} \quad (5)$$

where ω is the angular frequency ($\omega = 2\pi f$, and f is the frequency), j is the imaginary number ($j^2 = -1$), Y_o is the amplitude comparable to capacitance, and n is a dimensionless parameter comprised between 0 and 1, which can provide details about the degree of inhomogeneity of the metal surface.

There were two CPE, including the non-ideal coating capacitance (CPE_1) and double-layer capacitance (CPE_2) used in the model, as shown in Fig. 15(b). The fitting results are displayed in Table 3. Typically, higher R_{ct} values and lower electron transfer values indicate that the samples are less susceptible to corrosion in the corrosive environment [52]. In chloride-ion-containing solutions, chloride ions can erode the passivation film on the coating surface, leading to a decrease in the sample's impedance value. From the table, it is evident that the charge transfer resistance of the HEA-6 g/L-40 mA coating was the highest at 48,170 Ωcm^2, signifying a dense passivation film on its surface with relatively high protective properties. With increased Si_3N_4 particle loadings and deposition current densities, the surface microstructures of the coatings become increasingly uneven, and the ceramic particles tend to agglomerate, forming galvanic couples (with the Si_3N_4 particles having a higher corrosion potential as cathodes and the HEA matrix as anodes), ultimately resulting in a decline in the overall corrosion resistance of the HEA-composite coatings.

According to the electrochemical theory, the i_{corr} value is closely related to the surface roughness of the sample. When the sample surface is rough, the effective reaction area between the anode and cathode increases, leading to a higher corrosion current density [67]. As observed by SEM (Figs. 2 and 3), samples obtained under high ceramic loadings and great current densities exhibit larger surface roughness. Therefore, the actual corrosion-current densities of the composite coatings should be somewhat smaller than the corrosion-current-density values obtained from Tafel tests when considering the factor of surface roughness. In general, HEA coatings incorporated with Si_3N_4 particles demonstrate superior corrosion resistance compared to the pristine HEA coating when the influence of roughness is taken into account. HEA nanocomposite coatings exhibit significantly enhanced corrosion resistance, attributed to the following factors. (a). The presence of ceramic particles, which could serve as a physical barrier, contributes to the coatings' corrosion resistance [68]. (b). The dispersion of ceramic nanoparticles within the HEA matrix can induce structural changes by turning the columnar microstructure into equiaxed grains and blocking the propagation of corrosion paths, enhancing the anti-corrosion resistance of the composite coatings [45]. (c). The Si_3N_4 particles in the electrolyte solution could diminish defects, such as holes and pits that may arise from H_2 gas adhering to the growing front during electrodeposition, as depicted in Fig. 2, resulting in a denser, pore-free microstructure that enhances the overall corrosion resistance [69].

The general corrosion mechanism during the electrochemical test in a 3.5 wt% NaCl solution for the HEA-composite coatings could be described separately in terms of cathodic and anodic processes. The

Table 3
Corrosion parameters determined from the polarization tests and fitting of impedance spectra in a 3.5 wt % NaCl solution.

Samples	E_{corr} (V)	i_{corr}(μA/cm^2)	β_a(V/dec)	β_c(V/dec)	CPE (Ω^{-1} S^{-n}cm^2)	R_{ct} (Ωcm^2)	n
0g-40 mA	−0.2512	0.0795	0.0482	0.1231	7.4322	31,175	0.90
3g-20 mA	−0.2597	0.1237	0.0898	0.2129	14.129	54,596	0.92
3g-40 mA	−0.2599	0.0612	0.0521	0.1095	12.371	71,638	0.90
3g-60 mA	−0.2069	0.7791	0.0481	0.1229	34.809	16,950	0.85
6g-20 mA	−0.2347	0.0617	0.0771	0.1221	48.862	14,680	0.82
6g-40 mA	−0.2553	0.0518	0.0358	0.0786	7.7551	18,9940	0.94
6g-60 mA	−0.2247	0.0423	0.0525	0.0975	6.4292	29,3550	0.95
10g-20 mA	−0.2831	0.1134	0.0472	0.0991	9.8214	77,556	0.92
10g-40 mA	−0.2837	0.0943	0.1358	0.1078	11.416	46,552	0.89
10g-60 mA	−0.2891	0.1241	0.0707	0.0988	14.381	32,783	0.88

cathodic process might be composed of reduction of hydrogen and reduction of dissolved oxygen, as depicted by the following equations:

$$2H^+ + 2e^- \rightarrow H_2 \quad (6)$$

$$O_2 + 2H_2O + 4e^- \rightarrow 4OH^- \quad (7)$$

The anodic corrosion reaction, which is composed of the dissolution of the multi-alloying elements, can be described as follows [70]:

$$Ni = Ni^{2+} + 2e^- \quad (8)$$

$$Co = Co^{2+} + 2e^- \quad (9)$$

$$Fe = Fe^{2+} + 2e^- \quad (10)$$

$$Cu = Cu^{2+} + 2e^- \quad (11)$$

It is worthy to point out that when the sample surface underwent corrosion, it could be considered to be composed of numerous surface micro-galvanic cells. Silicon nitride, due to its inert chemical properties, can be regarded as the cathode of the corrosion cell, while the HEA alloy matrix acts as the anode. Additionally, because copper (Cu) has the highest electrode potential, the reaction current for Cu during corrosion should be the least.

Corrosion resistance stands as a critical performance metric for electrodeposited HEA coatings designed for protective applications. Previous research featured the incorporation of inert reinforcing agents like the graphene oxide (GO) and carbon nanotubes (CNT) to bolster the stability of the HEA matrix and enhance its corrosion resistance [47,48]. These reinforcements facilitate the formation of stable oxide layers on the HEA coating surface, impeding attacking ions, such as chloride cations, and notably improving corrosion resistance compared to unreinforced HEA coatings [48]. However, currently, very few researchers have used inexpensive ceramic particles as reinforcing phases to prepare and study the microstructures and properties of electrodeposited high-entropy alloy composites. Dehestani et al. examined SiC particle-reinforced FeCoNiWMo high-entropy alloy coatings, demonstrating that adding 20 g/L of SiC particles significantly enhances the hardness, wear resistance, and corrosion resistance of high-entropy alloys [40]. The present experimental results indicate that incorporating a small amount of Si_3N_4 ceramic particles can obviously improve the wear resistance and corrosion resistance of composite coatings. These studies all highlight the feasibility and superior performance of electrodeposited ceramic-reinforced high-entropy alloy coatings, showing the practicality of electrodeposition processes and broad application prospects in the preparation of composite materials and surface protection for materials used in corrosive circumstances.

5. Conclusions

In the study, Si_3N_4 ceramic-enhanced NiFeCoCu nanocomposite coatings were fabricated by electro-co-deposition with varying ceramic loadings and current densities, and the main findings are summarized as follows.

1. By increasing the current density and ceramic loading in the electrolyte, the grain size in the ceramic coatings firstly decreases and then increases, leading to an increasing trend in the surface roughness of the deposits, particularly resulting in more heterogeneous surface topography in the composite coatings obtained under high current densities.
2. Within the 20–40 mA/cm^2 current-density range, the deposited composite coatings only consist of a single FCC phase, whereas when the electroplating current density is increased to 60 mA/cm^2, the composite coatings were made up of an FCC + BCC two-phase structure.
3. Compared to the pristine samples, the addition of Si_3N_4 particles in the matrix weakens the (311) texture, while enhancing the (111) and (200) textures.
4. The incorporation of Si_3N_4 obviously enhances the hardness and wear resistance of the HEA matrixes. For the HEA-3 g/L composite coatings, the friction coefficient is slightly reduced due to the lubricating effect of Si_3N_4. With grain refinement and increased hardness, the HEA-3 g/L samples exhibit the lowest wear volume and with a wear mechanism, which is a combination of adhesive and abrasive wear.
5. The addition of Si_3N_4 significantly improves the corrosion resistance of high-entropy alloy composite coatings in simulated seawater. The HEA-6 g/L series of composite coatings display the best corrosion resistance, attributed to the optimization of their morphologies and microstructures.
6. The present study suggests a promising industrial approach for preparing ceramic-enhanced HEA composite coatings, holding great potential for surface modification and protection of the engineering materials utilized in corrosive and wear conditions.

Data Availability statement

The data presented in this study are available on request from the corresponding author.

CRediT authorship contribution statement

Ying Wang: Conceptualization. **Bingyang Ma:** Validation. **Wei Li:** Project administration. **Peter K. Liaw:** Resources, Writing – original draft, Writing – review & editing. **Xiaodong Wang:** Investigation. **Songpu Yang:** Methodology. **Ning Zhong:** Supervision.

Declaration of competing interest

The authors declare the following financial interests/personal relationships which may be considered as potential competing interests:

Wei Li reports financial support was provided by National Natural Science Foundation of China. If there are other authors, they declare that they have no known competing financial interests or personal

relationships that could have appeared to influence the work reported in this paper.

Acknowledgments

The authors are grateful for the finance support by the National Natural Science Foundation of China (51971148), National Key R&D Program of China (No.2017YFB0703003), and Shanghai Engineering Technology Research Centre of Deep Offshore Material (19DZ2253100) and Hot Manufacturing (18DZ2253400). PKL very much appreciates the support from (1) the National Science Foundation (DMR—1611180, 1809640, and 2226508) and (2) the Army Research Office (W911NF-13–1-0438 and W911NF-19–2-0049).

References

[1] Murty BS, Yeh JW, Ranganathan S. High-entropy alloys. first ed. Oxford, UK: Butterworth-Heinemann; 2014.
[2] Cantor B, Chang ITH, Knight P, Vincent AJB. Microstructural development in equiatomic multicomponent alloys. Mater. Sci. Eng. A 2004;375–377:213–8. https://doi.org/10.1016/j.msea.2003.10.257.
[3] Yeh JW, Chen SK, Lin SJ, Gan JY, Chin TS, Shun TT, Tsau CH, Chang SY. Nanostructured high-entropy alloys with multiple principal elements: novel alloy design concepts and outcomes. Adv Eng Mater 2004;6:299–303. https://doi.org/10.1002/adem.200300567.
[4] Wang S, Li J, Li D. First-principle study on physical properties and vacancy formation of face-centered cubic Co–Ni–Cu–Mo–W high entropy alloys. J Mater Res Technol 2023;25:5483–93. https://doi.org/10.1016/j.jmrt.2023.07.005.
[5] Paul TR, Belova IV, Murch GE. Analysis of diffusion in high entropy alloys. Mater Chem Phys 2018;210:301–8. https://doi.org/10.1016/j.matchemphys.2017.06.039.
[6] Shi P, Li R, Li Y, Wen Y, Zhong Y, Ren W, Shen Z, Zheng T, Peng J, Liang X, Hu P, Min N, Zhang Y, Ren Y, Liaw PK, Raabe D, Wang YD. Hierarchical crack buffering triples ductility in eutectic herringbone high-entropy alloys. Science 2021;373:912–8. https://doi.org/10.1126/science.abf6986.
[7] Li W, Liu P, Liaw PK. Microstructures and properties of high-entropy alloy films and coatings: a review. Mater. Res. Lett. 2018;6:199–229. https://doi.org/10.1080/21663831.2018.1434248.
[8] Bhattacharyya JJ, Inman SB, Wischhusen MA, Qi J, Poon J, Scully JR, Agnew SR. Lightweight, low cost compositionally complex multiphase alloys with optimized strength, ductility and corrosion resistance: discovery, design and mechanistic understandings. Mater Des 2023;228:111831. https://doi.org/10.1016/j.matdes.2023.111831.
[9] Gludovatz B, Hohenwarter A, Catoor D, Chang EH, George EP, Ritchie RO. A fracture-resistant high-entropy alloy for cryogenic applications. Science 2014;345:1153–8. https://doi.org/10.1126/science.1254581.
[10] Pan Q, Zhang L, Feng R, Lu Q, An K, Chuang AC, Poplawsky JD, Liaw PK, Lu L. Gradient cell–structured high-entropy alloy with exceptional strength and ductility. Science 2021;374:984–9. https://doi.org/10.1126/science.abj8114.
[11] Soto AO, Salgado AS, Niño EB. Thermodynamic analysis of high entropy alloys and their mechanical behavior in high and low-temperature conditions with a microstructural approach - a review. Intermetallics 2020;124:106850. https://doi.org/10.1016/j.intermet.2020.106850.
[12] Ostovari Moghaddam A, Cabot A, Trofimov EA. Does the pathway for development of next generation nuclear materials straightly go through high-entropy materials? Int J Refract Met Hard Mater 2021;97:105504. https://doi.org/10.1016/j.ijrmhm.2021.105504.
[13] Wan Y, Cheng Y, Chen Y, Zhang Z, Liu Y, Gong H, Shen B, Liang X. A nitride-reinforced NbMoTaWHfN refractory high-entropy alloy with potential ultra-high-temperature engineering applications. Engineering 2023;30:110–20. https://doi.org/10.1016/j.eng.2023.06.008.
[14] Oses C, Toher C, Curtarolo S. High-entropy ceramics. Nat Rev Mater 2020;5:295–309. https://doi.org/10.1038/s41578-019-0170-8.
[15] Sarkar A, Wang Q, Schiele A, Chellali MR, Bhattacharya SS, Wang D, Brezesinski T, Hahn H, Velasco L, Breitung B. High-entropy oxides: fundamental aspects and electrochemical properties. Adv. Mater. 2019;31:1806236. https://doi.org/10.1002/adma.201806236.
[16] Hu J, Yang Q, Zhu S, Zhang Y, Yan D, Gan K, Li Z. Superhard bulk high-entropy carbides with enhanced toughness via metastable in-situ particles. Nat Commun 2023;14:1–12. https://doi.org/10.1038/s41467-023-41481-6.
[17] Rao P, Deng Y, Fan W, Luo J, Deng P, Li J, Shen Y, Tian X. Movable type printing method to synthesize high-entropy single-atom catalysts. Nat Commun 2022;13:1–9. https://doi.org/10.1038/s41467-022-32850-8.
[18] Schweidler S, Botros M, Strauss F, Wang Q, Ma Y, Velasco L, Cadilha Marques G, Sarkar A, Kübel C, Hahn H, Aghassi-Hagmann J, Brezesinski T, Breitung B. High-entropy materials for energy and electronic applications. Nat Rev Mater 2024;9:266–81. https://doi.org/10.1038/s41578-024-00654-5.
[19] Yang B, Zhang Y, Pan H, Si W, Zhang Q, Shen Z, Yu Y, Lan S, Meng F, Liu Y, Huang H, He J, Gu L, Zhang S, Chen LQ, Zhu J, Nan CW, Lin YH. High-entropy enhanced capacitive energy storage. Nat Mater 2022;21:1074–80. https://doi.org/10.1038/s41563-022-01274-6.
[20] Wang YT, Li JB, Xin YC, Chen XH, Rashad M, Liu B, Liu Y. Hot deformation behavior and hardness of a CoCrFeMnNi high-entropy alloy with high content of carbon. Acta Metall. Sin. Engl. Lett. 2019;32:932–43. https://doi.org/10.1007/s40195-019-00916-0.
[21] Xu F, Ding N, Li N, Liu L, Hou N, Xu N, Guo W, Tian L, Xu H, Lawrence Wu CM, Wu X, Chen X. A review of bearing failure Modes, mechanisms and causes. Eng Fail Anal 2023;152:107518. https://doi.org/10.1016/j.engfailanal.2023.107518.
[22] Shi Y, Yang B, Xie X, Brechtl J, Dahmen KA, Liaw PK. Corrosion of AlxCoCrFeNi high-entropy alloys: Al-content and potential scan-rate dependent pitting behavior. Corros. Sci. 2017;119:33–45. https://doi.org/10.1016/j.corsci.2017.02.019.
[23] Lingling Y, Yanjie Z, Haokai L, Tao G, Hui T, Shuangdong Y, Yu L, Hongguang W, Yanli L, Jiuming M, Dong W. Co-deposition and thermal conductivity of nickel–graphene composite coatings on copper surface. Appl. Phys. A 2023;129:757. https://doi.org/10.1007/s00339-023-07022-0.
[24] Zhang HX, Dai JJ, Sun CX, Li SY. Plasma spraying. J Mater Process Technol 2020;282:116671. https://doi.org/10.1016/j.jmatprotec.2020.116671.
[25] Zhang S, Li W, Hu Y, Jiang T, Guo L, Zhang Y, Zhao Y. Effect of spraying power on the microstructure and wear behavior of the plasma-sprayed FeCoCrNiMo 0.2 coating. AIP Adv 2021;11:115110. https://doi.org/10.1063/5.0074776.
[26] Meghwal A, Anupam A, Murty BS, Berndt CC, Kottada RS, Ang ASM. Thermal spray high-entropy alloy coatings: a Review. J Therm Spray Technol 2020;29:857–93. https://doi.org/10.1007/s11666-020-01047-0.
[27] Haché MJR, Tam J, Erb U, Zou Y. Electrodeposited NiFeCo-(Mo,W) high-entropy alloys with nanocrystalline and amorphous structures. J Alloys Compd 2023;952:170026. https://doi.org/10.1016/j.jallcom.2023.170026.
[28] Wang J, Fan J, Li W, Liu P, Ma X, Zhang K, Ma F, Chen X, Liaw PK. Effects of nitrogen content on microstructures and mechanical behavior of (TiTaCrMoNb)Nx films. Mater. Sci. Eng. 2023;A:145331. https://doi.org/10.1016/j.msea.2023.145331.
[29] Jin B, Zhang N, Yu H, Hao D, Ma Y. AlxCoCrFeNiSi high entropy alloy coatings with high microhardness and improved wear resistance. Surf Coat Technol 2020;402:126328. https://doi.org/10.1016/j.surfcoat.2020.126328.
[30] Aliyu A, Srivastava C. Corrosion behavior and protective film constitution of AlNiCoFeCu and AlCrNiCoFeCu high entropy alloy coatings. Surf. Interfaces 2021;27:101481. https://doi.org/10.1016/j.surfin.2021.101481.
[31] Ahmadkhaniha D, Kruemmling J, Zanella C. Electrodeposition of high entropy alloy of Ni-Co-Cu-Mo-W from an aqueous bath. J Electrochem Soc 2022;169:082515. https://doi.org/10.1149/1945-7111/ac87d5.
[32] Dehestani M, Sharafi S, Khayati GR. The effect of pulse current density on the microstructure, magnetic, mechanical, and corrosion properties of high-entropy alloy coating Fe–Co–Ni–Mo–W, achieved through electro co-deposition. Intermetallics 2022;147:107610. https://doi.org/10.1016/j.intermet.2022.107610.
[33] Wang Y, Ma B, Li W, Liaw PK, Yang S, Zhong N. Effect of additive and current density on microstructures and corrosion behavior of a multi-component NiFeCoCu alloy prepared by electrodeposition. Crystals 2024;14:171. https://doi.org/10.3390/cryst14020171.
[34] Popescu AMJ, Branzoi F, Constantin I, Anastasescu M, Burada M, Mitrică D, Anasiei I, Olaru MT, Constantin V. Electrodeposition, characterization, and corrosion behavior of CoCrFeMnNi high-entropy alloy thin films. Coatings 2021;11:1367. https://doi.org/10.3390/coatings11111367.
[35] Yoosefan F, Ashrafi A, Monir Vaghefi SM. Characterization of Co-Cr-Fe-Mn-Ni high-entropy alloy thin films synthesized by pulse electrodeposition: Part 2: effect of pulse electrodeposition parameters on the wettability and corrosion resistance. Met Mater Int 2021;27:106–17. https://doi.org/10.1007/s12540-019-00584-w.
[36] Pavithra CLP, Janardhana RKSK, Reddy KM, Murapaka C, Wang X, Dey SR. One-dimensional Co-Cu-Fe-Ni-Zn high-entropy alloy nanostructures. Mater. Res. Lett. 2021;9:285–90. https://doi.org/10.1080/21663831.2021.1896588.
[37] Nagy P, Péter L, Czigány Z, Chinh NQ, Gubicza J. Processing and characterization of an electrodeposited nanocrystalline Co–Fe–Ni–Zn multi-principal element alloy film. Surf Coat Technol 2023;467:129740. https://doi.org/10.1016/j.surfcoat.2023.129740.
[38] Freitas GFN, Gomes WS, Souza JPI, Pinotti CN, Passamani EC, Montemor MF, Della Noce R. Direct electrodeposition of CoFeNiMoW high entropy alloy thin films from aqueous medium. Mater Chem Phys 2023;309:128438. https://doi.org/10.1016/j.matchemphys.2023.128438.
[39] Bian HW, Wang R, Zhang KZ, Zheng HL, Wen MJ, Li ZM, Li ZH, Wang GX, Xie GW, Liu X, Jiang LH. Facile electrodeposition synthesis and super performance of nanoporous Ni-Fe-Cu-Co-W high entropy alloy electrocatalyst. Surf. Coat Technol. 2023.
[40] Dehestani M, Sharafi S, Khayati GR. Electrodeposited FeCoNiWMo high entropy alloy/SiC nanocomposite coatings: microstructure, mechanical properties and corrosion resistance. Intermetallics 2023;162:107988. https://doi.org/10.1016/j.intermet.2023.107988.
[41] Jarzabek DM, Chmielewski M, Dulnik J, Strojny-Nedza A. The influence of the particle size on the ddhesion between ceramic particles and metal matrix in MMC composites. J Mater Eng Perform 2016;25:3139–45. https://doi.org/10.1007/s11665-016-2107-3.
[42] Shirvanimoghaddam K, Khayyam H, Abdizadeh H, Karbalaei Akbari M, Pakseresht AH, Abdi F, Abbasi A, Naebe M. Effect of B_4C, TiB_2 and $ZrSiO_4$ ceramic particles on mechanical properties of aluminium matrix composites: experimental investigation and predictive modelling. Ceram Int 2016;42:6206–20. https://doi.org/10.1016/j.ceramint.2015.12.181.
[43] Dorri Moghadam A, Schultz BF, Ferguson JB, Omrani E, Rohatgi PK, Gupta N. Functional metal matrix composites: self-lubricating, self-healing, and nanocomposites-An outlook. JOM 2014;66:872–81. https://doi.org/10.1007/s11837-014-0948-5.

[44] Kumaraguru S, Sundaravadivel E. Direct electro-synthesis of rationally designed, sturdy Ni–P–Bi_2O_3 nanocomposite coatings: tailoring the texture, microhardness, and corrosion prevention characteristics. Ceram Int 2022;48:28864–73. https://doi.org/10.1016/j.ceramint.2022.03.283.
[45] Karimzadeh A, Aliofkhazraei M, Walsh FC. A review of electrodeposited Ni-Co alloy and composite coatings: microstructure, properties and applications. Surf Coat Technol 2019;372:463–98. https://doi.org/10.1016/j.surfcoat.2019.04.079.
[46] Aliyu A, Srivastava C. Phase constitution, surface chemistry and corrosion behavior of electrodeposited MnFeCoNiCu high entropy alloy-graphene oxide composite coatings. Surf Coat Technol 2022;429:127943. https://doi.org/10.1016/j.surfcoat.2021.127943.
[47] Pavithra CLP, Janardhana RKSK, Reddy KM, Murapaka C, Klement U, Dey SR. Graphene oxide reinforced magnetic FeCoNiCuZn high entropy alloy through electrodeposition. J Electrochem Soc 2022;169:022501. https://doi.org/10.1149/1945-7111/ac4e56.
[48] Rao P, Singh S, Kumar K, Pandel U, Srivastava C. Understanding the evolution of microstructure, phase homogeneity, electrochemical characteristics and surface chemistry of electrodeposited MnCrCoFeNiCu high entropy alloy coating with reinforcement of carbon nanotubes. Surf Coat Technol 2023;471:129912. https://doi.org/10.1016/j.surfcoat.2023.129912.
[49] Kleebe HJ, Pezzotti G, Ziegler G. Microstructure and fracture toughness of Si_3N_4 ceramics: combined roles of grain morphology and secondary phase chemistry. J Am Ceram Soc 1999;82:1857–67. https://doi.org/10.1111/j.1151-2916.1999.tb02009.x.
[50] Haché MJR, Zou Y, Erb U. Post-deposition crack evolution in Cr(III) alloy electrodeposits: phenomenology. Surf Coat Technol 2021;406:126648. https://doi.org/10.1016/j.surfcoat.2020.126648.
[51] Klug HP, Alexander AL. X-ray diffraction procedures: for polycrystalline and amorphous materials. second ed. John Wiley and Sons; 1974.
[52] McCafferty E. Validation of corrosion rates measured by the Tafel extrapolation method. Corros. Sci. 2005;47:3202–15. https://doi.org/10.1016/j.corsci.2005.05.046.
[53] Liu Q, Zhou B, Zhang J, Zhang W, Zhao M, Li N, Xiong M, Chen J, Yu Y, Song S. Influence of Ru-Ni-Nb combined cathode modification on corrosion behavior and passive film characteristics of Ti-6Al-4V Alloy used for oil country tubular goods. Corros. Sci. 2022;207:110569. https://doi.org/10.1016/j.corsci.2022.110569.
[54] Sajjadnejad M, Haghshenas SMS, Badr P, Setoudeh N, Hosseinpour S. Wear and tribological characterization of nickel matrix electrodeposited composites: a review. Wear 2021;486–487:204098. https://doi.org/10.1016/j.wear.2021.204098.
[55] Guglielmi N. Kinetics of the deposition of inert particles from electrolytic baths. J Electrochem Soc 1972;119:1009. https://doi.org/10.1149/1.2404383.
[56] Zhang Z, Xian J, Wu H, Jin M, Shen Z. Influence of particle concentration on the elemental penetration region and properties of Ni-P-SiC composite coatings prepared through sandblasting and scanning electrodeposition on 45 steel surfaces. Coatings 2021;11:1237. https://doi.org/10.3390/coatings11101237.
[57] Wang L, Ren J, Zhao Y, Ji V, Huabing L, Liu M, Wang Z, Jiang C, Zhanyong W. Effect of Ti microparticles on the microstructure and properties of Ni-Ti composite coating prepared by electrodeposition. J Alloys Compd 2022;908:164313. https://doi.org/10.1016/j.jallcom.2022.164313.
[58] Ghavidel N, Allahkaram SR, Naderi R, Barzegar M, Bakhshandeh H. Corrosion and wear behavior of an electroless Ni-P/nano-SiC coating on AZ31 Mg alloy obtained through environmentally-friendly conversion coating. Surf Coat Technol 2020;382:125156. https://doi.org/10.1016/j.surfcoat.2019.125156.
[59] Tokarewicz M, Gradzka-Dahlke M. Review of recent research on AlCoCrFeNi high-entropy alloy. Metals 2021;11:1302. https://doi.org/10.3390/met11081302.
[60] Sajjadnejad M, Abadeh HK, Omidvar H, Hosseinpour S. Assessment of Tribological behavior of nickel-nano Si_3N_4 composite coatings fabricated by pulsed electroplating process. Surf Topogr Metrol Prop 2020;8:025009. https://doi.org/10.1088/2051-672X/ab7ae5.
[61] Zhang Y, Zuo TT, Tang Z, Gao MC, Dahmen KA, Liaw PK, Lu ZP. Microstructures and properties of high-entropy alloys. Prog Mater Sci 2014;61:1–93. https://doi.org/10.1016/j.pmatsci.2013.10.001.
[62] Petrović Ž, Metikoš-Huković M, Grubač Z, Omanović S. The nucleation of Ni on carbon microelectrodes and its electrocatalytic activity in hydrogen evolution. Thin Solid Films 2006;513:193–200. https://doi.org/10.1016/j.tsf.2006.01.026.
[63] Singh S, Sribalaji M, Wasekar NP, Joshi S, Sundararajan G, Singh R, Keshri AK. Microstructural, phase evolution and corrosion properties of silicon carbide reinforced pulse electrodeposited nickel–tungsten composite coatings. Appl Surf Sci 2016;364:264–72. https://doi.org/10.1016/j.apsusc.2015.12.179.
[64] Li Z, Ma F, Li D, Wan S, Yi G, Geng G, Guo L. Enhanced mechanical and tribological capabilities of a silicon aluminum alloy with an electroplated Ni-Co-P/Si_3N_4 composite coating. Metals 2022;12. https://doi.org/10.3390/met12010120.
[65] Frérot L, Aghababaei R, Molinari J-F. A mechanistic understanding of the wear coefficient: from single to multiple asperities contact. J. Mech. Phys. Solids 2018;114:172–84. https://doi.org/10.1016/j.jmps.2018.02.015.
[66] Chi H, Jiang L, Chen G, Qiao J, Lin X, Wu G. The tribological behavior evolution of TiB_2/Al composites from running-in stage to steady stage. Wear 2016;368–369:304–13. https://doi.org/10.1016/j.wear.2016.10.003.
[67] Paknahad H, Shahriari Nogorani F. Corrosion behavior of low-temperature nickel and iron aluminized martensitic stainless steel substrates with different surface roughness in acidic medium. J Mater Eng Perform 2023;32:1874–82. https://doi.org/10.1007/s11665-022-07240-2.
[68] Reddy RM, Praveen BM, Chandrappa KG, Nayana KO. Generation of Ni–Si3N4 nanocomposites by DC, PC and PRC electrodeposition methods. Surf Eng 2016;32:501–7. https://doi.org/10.1080/02670844.2016.1148323.
[69] Hosseini MG, Ahmadiyeh S, Rasooli A. Pulse plating of Ni–B/WC nanocomposite coating and study of its corrosion and wear resistance. Mater Sci Technol 2019;35:1248–56. https://doi.org/10.1080/02670836.2019.1619292.
[70] Electrochemical kinetics of the high entropy alloys in aqueous environments—a comparison with type 304 stainless steel. Corros. Sci. 2005;47:2679–99. https://doi.org/10.1016/j.corsci.2004.09.026.